RSC Advances

PAPER

View Article Online
View Journal | View Issue

Cite this: *RSC Adv.*, 2020, **10**, 6035

Synthesis of hierarchical Sn/SnO nanosheets assembled by carbon-coated hollow nanospheres as anode materials for lithium/sodium ion batteries

Fengrong He,[a] Qi Xu,*[b] Baoping Zheng,[a] Jun Zhang,[c] Zhenguo Wu,[b] Yanjun Zhong,[b] Yanxiao Chen,[b] Wei Xiang,[d] Benhe Zhong[b] and Xiaodong Guo*[be]

Tin-based anode materials have aroused interest due to their high capacities. Nevertheless, the volume expansion problem during lithium insertion/extraction processes has severely hindered their practical application. In particular, nano–micro hierarchical structure is attractive with the integrated advantages of nano-effect and high thermal stability of the microstructure. Herein, hierarchical Sn/SnO nanosheets assembled by carbon-coated hollow nanospheres were successfully synthesized by a facile glucose-assisted hydrothermal method, in which the glucose served as both morphology-control agent and carbon source. The hierarchical Sn/SnO nanosheets exhibit excellent electrochemical performances owing to the unique configuration and carbon coating. Specifically, a reversible high capacity of 2072.2 mA h g^{-1} was observed at 100 mA g^{-1}. Further, 964.1 mA h g^{-1} after 100 cycles at 100 mA g^{-1} and 820.4 mA h g^{-1} at 1000 mA g^{-1} after 300 cycles could be obtained. Encouragingly, the Sn/SnO also presents certain sodium ion storage properties. This facile synthetic strategy may provide new insight into fabricating high-performance Sn-based anode materials combining the advantages of both structure and carbon coating.

Received 29th October 2019
Accepted 14th January 2020

DOI: 10.1039/c9ra08897k

rsc.li/rsc-advances

1. Introduction

Currently, considerable attention has been paid to lithium ion batteries (LIBs) for their promising application in hybrid electric vehicles (HEVs), electric vehicles (EVs) and large-scale renewable energy storage systems owing to their high energy density, long life span and relatively low environmental impacts.[1–4] Although graphite is extensively employed as an anode, its limited theoretical density (372 mA h g^{-1}) prevents it from meeting the ever-increasing requirements for higher power and energy density.[5] Thus, tremendous efforts have been devoted to develop new anodes with higher specific capacity and excellent cycle stability for next-generation LIBs.[6–10] Among them, tin-based anode materials have been regarded as potential candidates with high theoretical capacity (Sn: 994 mA h g^{-1}; SnO: 875 mA h g^{-1}; SnO_2: 783 mA h g^{-1}), natural abundance and environmental benignity.[11,12] Unfortunately, Sn-based anodes inevitably suffer from pulverization and aggregation problems caused by the large volume variation (>300%) during lithiation–delithiation processes, which would lead to the loss of interparticle contact and consequently rapid capacity fading during cycling processes.[13,14]

Substantial significant research studies have been focused on overcoming these problems. One effective strategy is to design various nanostructures to alleviate the mechanical strain and shorten the electron and ion diffusion lengths. A variety of novel nanostructures including nanowires,[15,16] nanosheets,[17,18] nanoboxes,[19] nanotubes[20,21] and hollow nanospheres[22–24] have been explored. Particularly, hierarchically porous nanostructures such as hollow nanospheres have drawn extensive interest due to their peculiar hollow interior, which can provide large contact area and short diffusion path as well as sustain the huge volume change, thereby improving the cycling stability. For example, Gurunathan *et al.*[25] have synthesized hierarchically porous SnO_2 hollow microspheres (HMS) by employing the resorcinol–formaldehyde (RF) gel method. An initial discharge capacity of 800 mA h g^{-1} and 79% capacity retention could be delivered at 1C rate after 100 cycles when using Na-alginate as binder. Another available method is to introduce a carbon layer, which can not only buffer the volume expansion but also improve the electrical conductivity. For instance, Li and co-workers[26] have designed SnO_2 nanospheres with oxygen vacancies encapsulated in the N-doped graphene

[a]*Dong guan Hec Technology Research Corporation, Dongguan, Guangdong 523871, P. R. China*
[b]*School of Chemical Engineering, Sichuan University, Chengdu 610065, P. R. China. E-mail: xiaodong2009@scu.edu.cn*
[c]*Ruyuan Dongyangguang Magnetic Material Limited Company, Shaoguan, Guangdong 512710, P. R. China*
[d]*College of Materials and Chemistry & Chemical Engineering, Chengdu University of Technology, Chengdu 610059, P. R. China*
[e]*Institute for Superconducting and Electronic Materials, University of Wollongong, Wollongong, NSW 2522, Australia*

hierarchical network by an electrostatic adsorption-induced self-assembled together with a thermal reduction process. The as-prepared sample exhibits excellent lithium storage properties with a high reversible capacity of 912 mA h g^{-1} at the end of 200 cycles at 0.5 A g^{-1} and 652 mA h g^{-1} at the end of 200 cycles at 1 A g^{-1}. However, the synthesis of hollow structures is generally complicated and difficult to realize the structure design and carbon coating in a one-step process. Therefore, it is highly desirable to develop more efficient methods to fabricate materials integrating the advantages of both structure and carbon coating.

Although LIBs have dominated the portable electronics market in the past two decades, the high cost and limited lithium reserves potentially hinder their large-scale application from a long-time prospective.[27,28] In this context, sodium ion batteries (SIBs) have emerged as promising alternatives owing to the advantage of natural abundance, even distribution, and lower cost of Na resources.[29,30] Despite the similarity between Li-ion and Na-ion intercalation chemistry, graphite, which is commercially applied as an anode material for LIBs, is not a suitable option for SIBs due to sodium's unique characteristics.[31,32] According to some previous reports, Sn-based materials are considered to be prospective SIB anodes.[33,34] Zhang and co-workers[35] have prepared SnO nanosheets with controlled number of atomic layers and lateral size. A high reversible capacity of 665 mA h g^{-1} after 100 cycles at 0.1 A g^{-1} and 452 mA h g^{-1} after 1000 cycles at a high current density of 1.0 A g^{-1} was delivered, with superior rate capability. Qin *et al.*[36] obtained tetrahedral SnO microflowers by means of an ultrafast ionic liquid-assisted microwave method. The as-prepared SnO anode exhibits high average coulombic efficiency (CE) (98.5% for 50 cycles at a specific current of 100 mA g^{-1}) together with an unprecedented capacity contribution in the low potential region (5 mV to 0.5 V *vs.* Na/Na^+).

In this work, integrating the two typical strategies mentioned above, we successfully designed a hierarchical structure of Sn/SnO nanosheets composed of carbon-coated hollow nanospheres by a facile glucose-assisted hydrothermal method. The as-prepared Sn/SnO sample exhibits outstanding lithium-storage properties due to the unique configuration and carbon coating layer. A high reversible capacity of 964.1 mA h g^{-1} after 100 cycles at 100 mA g^{-1} and 820.4 mA h g^{-1} at 1000 mA g^{-1} after 300 cycles could be obtained. Surprisingly, the as-prepared sample also presents certain sodium ion battery properties. It's expected that this facile synthetic strategy could open a new sight into fabricating high-performance anode materials combining the advantages of both structure and carbon coating.

2. Experimental section

2.1. Synthesis of hierarchical Sn/SnO nanosheets

All chemicals were analytically pure and used directly without further purification. The hierarchical Sn/SnO nanosheets were prepared *via* a simple glucose-assisted hydrothermal treatment of commercial Sn nanoparticles (Nanjing Emperor Nano Material Co., Ltd, Nanjing, China). In a typical procedure, 2 g Sn nanoparticles and 6 g glucose (Sinopharm Chemical Reagent Co. Ltd, Shanghai, China) were mixed in 60 ml deionized water under vigorous stirring. The resultant hybrid was transferred to an oven and then maintained at 180 °C for 4 h. After cooled down to room temperature, the product was obtained by centrifugation, washed several times with water and ethanol, and then dried at 80 °C in a vacuum oven for 12 h.

2.2. Material characterization

The crystalline phase was identified by powder X-ray diffraction (XRD, Philips X'pert Pro Super X-ray diffractometer, Cu Kα radiation). The semi-quantitative XRD analysis is done by pattern simulation using Jade software. The morphology was investigated by field emission scanning electron microscopy (SEM, HITACHI S-4800) and transmission electron microscopy (TEM, JEM 2100). Nitrogen adsorption/desorption measurement was conducted on a Micromeritics Tristar 3000 system and the specific surface area was evaluated using the Brunauer–Emmett–Teller (BET) method. X-ray photoelectron spectroscopy (XPS) experiments were performed on a PHI QUANTUM 2000 instrument to determine the chemical composition of the samples.

2.3. Electrochemical measurements

The electrodes were prepared by spread the slurry of 75 wt% Sn/SnO active material, 15 wt% acetylene black and 10 wt% LA 132 (an acrylonitrile copolymer-based binder, Chengdu Indigo Power Source Co. Ltd.) onto copper foil current collectors, followed by drying at 80 °C overnight in a vacuum oven. The mass loading of the electrode is about 2.0 mg cm^{-2}. CR2025-type coin cells were employed to test the electrochemical properties of the electrodes. For lithium half-cells, lithium foil was served as the counter electrode and a polypropylene (PP) film (Celgard 2400) as the separator. The electrolyte consists of 1 M $LiPF_6$ and a mixture of ethylene carbonate (EC)/dimethyl carbonate (DMC)/diethyl carbonate (DEC) (volume ratio 1 : 1 : 1) with 2 wt% vinylene carbonate (VC) as the additive (Tinci Materials Technology Co., Ltd, Guangzhou, China). The sodium half-cells were assembled in a similar way. Metallic sodium and glass fiber (GF/A, Whatman) were utilized as the counter electrode and the separator, respectively. The electrolyte is composed of 1 M $NaPF_6$ and a mixture of EC/DEC (volume ratio 1 : 1) (Fosai New Materials Co., Ltd, Jiangsu, China). Galvanostatic charge–discharge tests were performed on a LAND-2001A battery test system (Land Electronic Co., Ltd, Wuhan, China). Cyclic voltammetry (CV) measurement was conducted on a CHI 660D electrochemical workstation (CH Instruments Co., Ltd, Shanghai, China).

3. Results and discussion

The crystalline structure and phase composition of the as-prepared sample were characterized by XRD pattern. As shown in Fig. 1a, the diffraction peaks can be indexed to tetragonal SnO with a space group of (129) *P*4/*nmm* (JCPDS card no. 78-1913) and tetragonal Sn with the space group (141) $I4_1/amd$ (JCPDS card no. 89-2958), indicating the presence of metallic Sn and SnO in the composite, while no peaks of other impurities were detected. In addition, the strong intensity and

sharpness of the diffraction peaks manifest good crystallinity of the sample. By means of semi-quantitative analysis of the XRD pattern, the mass ratio of SnO and Sn is determined to be about 89 : 11, indicating the dominance of SnO in the composite. The morphology and structure of the as-prepared Sn/SnO sample was investigated by SEM and TEM images. As depicted in Fig. 1b, the Sn/SnO composite consists of densely stacked nanosheets with a diameter of about 200 to 300 nm. A higher magnification image of the nanosheets (Fig. 1c) clearly presents a hierarchical structure composed of intimately interconnected nanospheres. TEM images display more details about the nanospheres. As can be seen from Fig. 1d, the Sn/SnO nanospheres have a hollow structure, with a diameter of about 30 nm. Additionally, a carbon shell with about 2 nm thickness can also be observed coating on the surface of nanospheres. In the representative HRTEM image (Fig. 1e), distinct crystal lattice with interplanar spacing of 0.311 nm and 0.318 nm are detected, corresponding to the (200) plane of Sn and (101) plane of SnO, respectively, further demonstrating the coexist of metallic Sn and SnO in the composite. The selected area electron diffraction (SAED) pattern (Fig. 1f) indicates the polycrystalline nature of the Sn/SnO sample. The several lattice fringes can be assigned to the (222) and (111) plane of SnO, and the (112) plane of Sn.

N_2 adsorption–desorption measurement was employed to estimate the specific surface area and pore characteristics of the

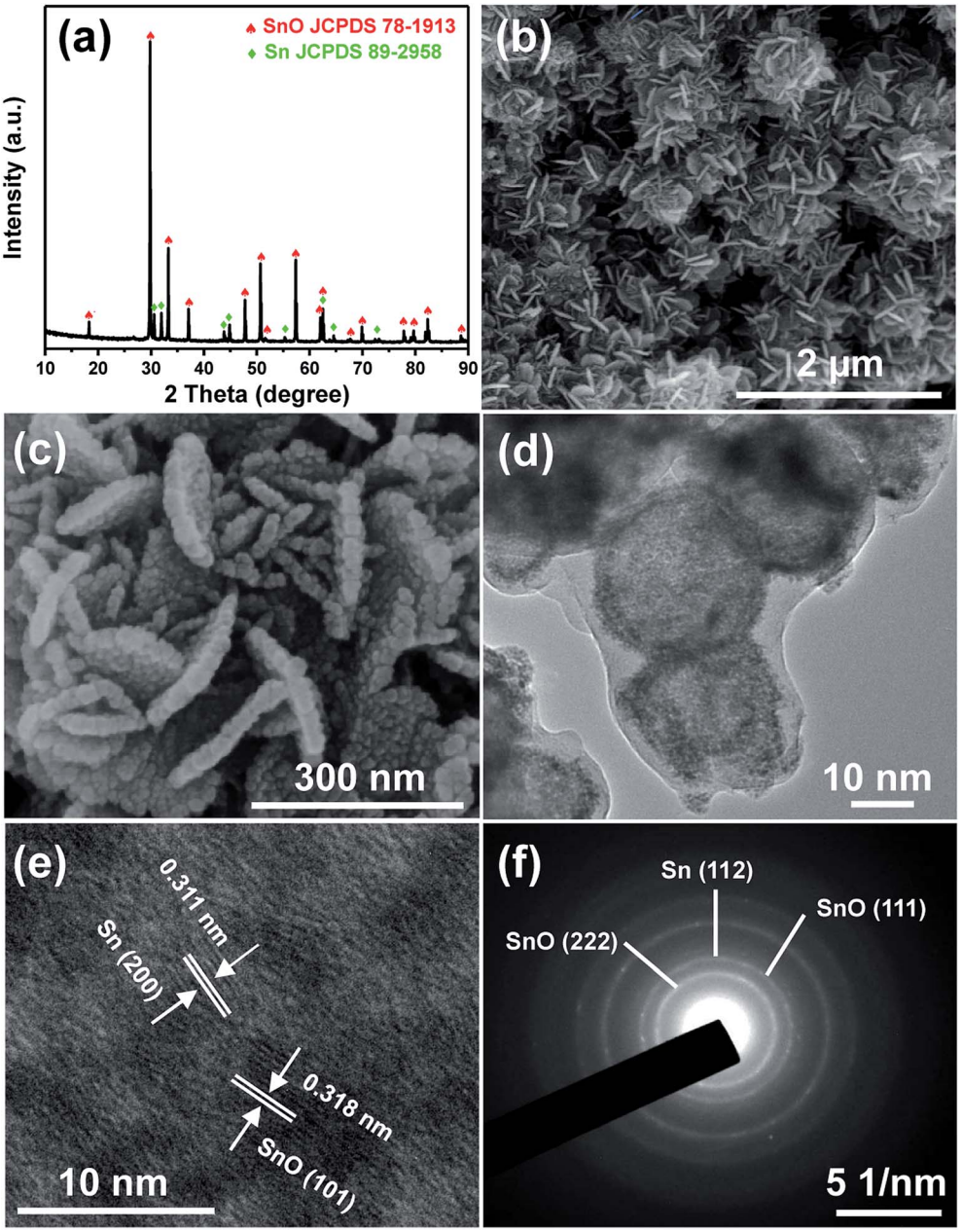

Fig. 1 (a) XRD pattern, (b and c) SEM images, (d) TEM image, (e) HRTEM image and (f) SAED pattern of the Sn/SnO sample.

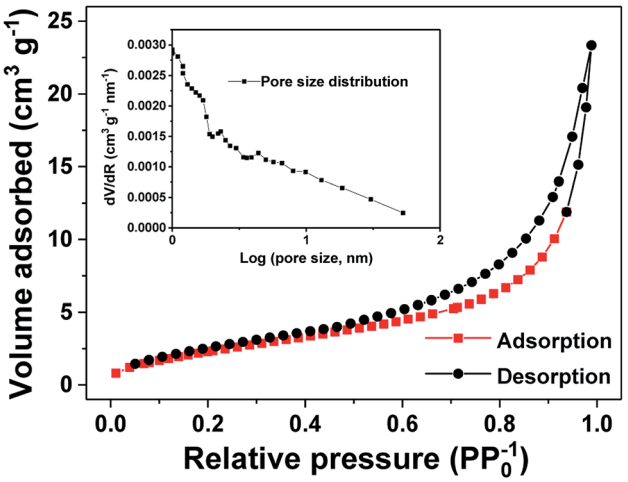

Fig. 2 N_2 adsorption–desorption isotherms and corresponding pore size distribution curve (the inset) of the Sn/SnO sample.

as-prepared Sn/SnO sample. As revealed in Fig. 2, the N_2 adsorption–desorption isotherm of the Sn/SnO nanosheets appears as a type-IV curve with an evident type H3 hysteresis loop, suggesting the formation of mesoporous structure. On the basis of the Brunauer–Emmett–Teller (BET) method, the as-prepared Sn/SnO sample delivers a specific surface area of 9.25 $m^2 g^{-1}$. The mean pore size and cumulative pore volume of the sample are about 7.18 nm and 0.035 nm, respectively, as calculated from the pore size distribution curve (the inset of Fig. 2) by Barrett–Joyner–Halendar (BJH) method. Such porous structure with internal void can not only provide large contact area for electrode and electrolyte but also accommodate the volume change of Sn/SnO nanosheet and facilitate the electrons and ions diffusion.[24,37]

XPS spectra were applied to study the chemical state on the surface of the as-prepared sample. The high-resolution spectrum of C 1s is depicted in Fig. 3a, which can be fitted into three peaks centered at 285.1, 286.7 and 288.4 eV, corresponding to C–C, C–O and C=O groups,[38] respectively. Fig. 3b displays the typical high-resolution spectrum of O 1s, there are four peaks located at 531.5, 531.9, 532.6 and 533.5 eV, which are assigned to O_2, Sn–O, H_2O and C–O, separately.[39] The Sn 3d spectrum (Fig. 3c) shows two peaks appearing at 487.6 eV (Sn $3d_{5/2}$) and 496.0 eV (Sn $3d_{3/2}$), which means that Sn exists principally in the form of tin oxide.[40,41]

The electrochemical performances of the Sn/SnO sample as anode material for LIBs are investigated. Fig. 4a shows the CV curves of the Sn/SnO sample in the potential window of 0–3.0 V (*vs.* Li/Li^+) at a scanning rate of 0.1 mV s^{-1} for the first three cycles. An irreversible reduction peak at 0.9 V can be observed during the first cathodic sweep, which is associated with the

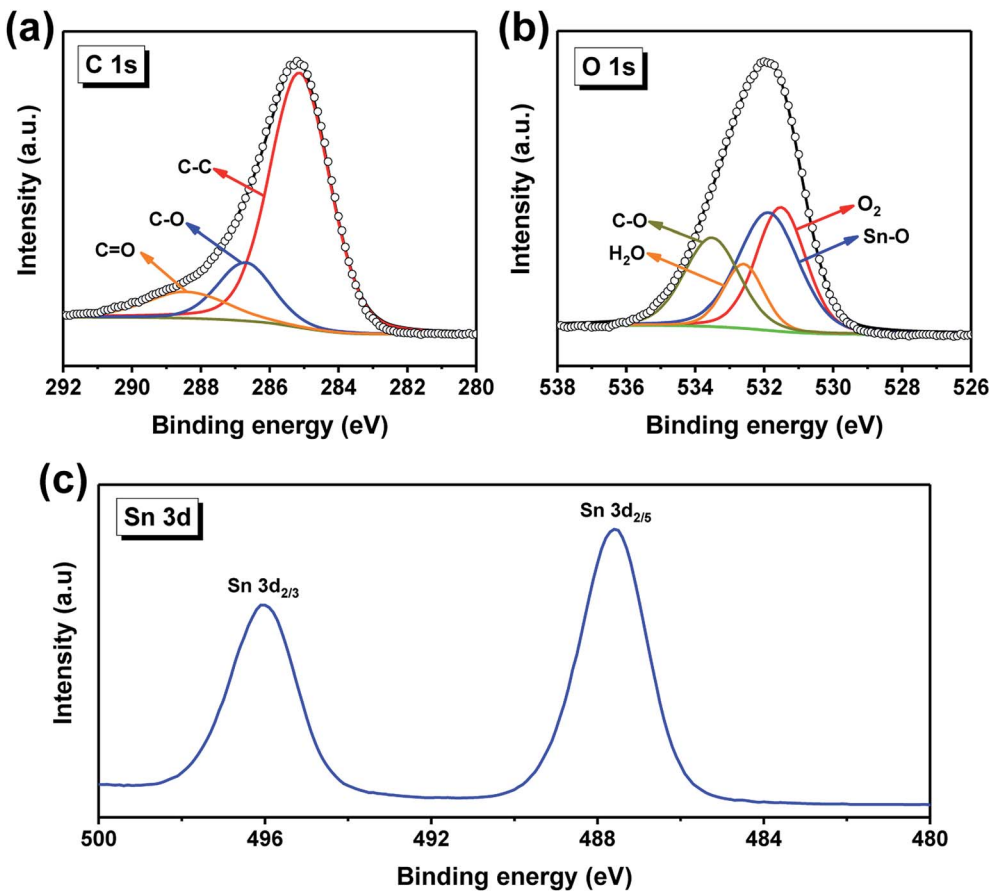

Fig. 3 XPS spectra of the Sn/SnO sample: (a) C 1s, (b) O 1s, (c) Sn 3d.

reduction of SnO to metallic Sn and the formation of a solid electrolyte interface (SEI) layer on the electrode surface.[42,43] The pronounced cathodic peak at the voltage close to 0.0 V can be ascribed to the alloying reaction of metallic Sn with lithium to form Li_xSn. In the following anodic scan, a strong peak at 0.6 V and a broad peak at 1.27 V can be detected, corresponding to the dealloying reaction of Li_xSn and partial reversible formation of SnO, respectively, consistent with the Sn-based anodes reported previously.[44,45] Besides, the CV curves almost overlap in the subsequent cycles, indicating the formation of stable SEI film and good reversibility of the electrochemical reactions in the electrode.

Fig. 4b shows the galvanostatic charge–discharge profiles of the Sn/SnO nanosheets electrode for the first three cycles at a current density of 100 mA g^{-1} in a voltage window of 0.01–3 V (*vs.* Li^+/Li). The initial charge and discharge capacities are 1137.2 mA h g^{-1} and 2072.2 mA h g^{-1}, corresponding to an initial coulombic efficiency (ICE) of 54.9%. Note that the specific capacity was calculated on the basis of the total mass of the Sn/SnO composite, including the negligible capacity supported by carbon. The large initial irreversible capacity loss (45.1%) could be attributed to the formation of SEI layer on the electrode surface and the decomposition of the electrolyte.[11,26] After the first cycle, the CE climbs to 91.6% and 93.6% in the 2nd and 3rd cycles, respectively, indicating the formation of a stable SEI film.

The cycling performance of the as-prepared Sn/SnO sample at a current density of 100 and 1000 mA g^{-1} are presented in

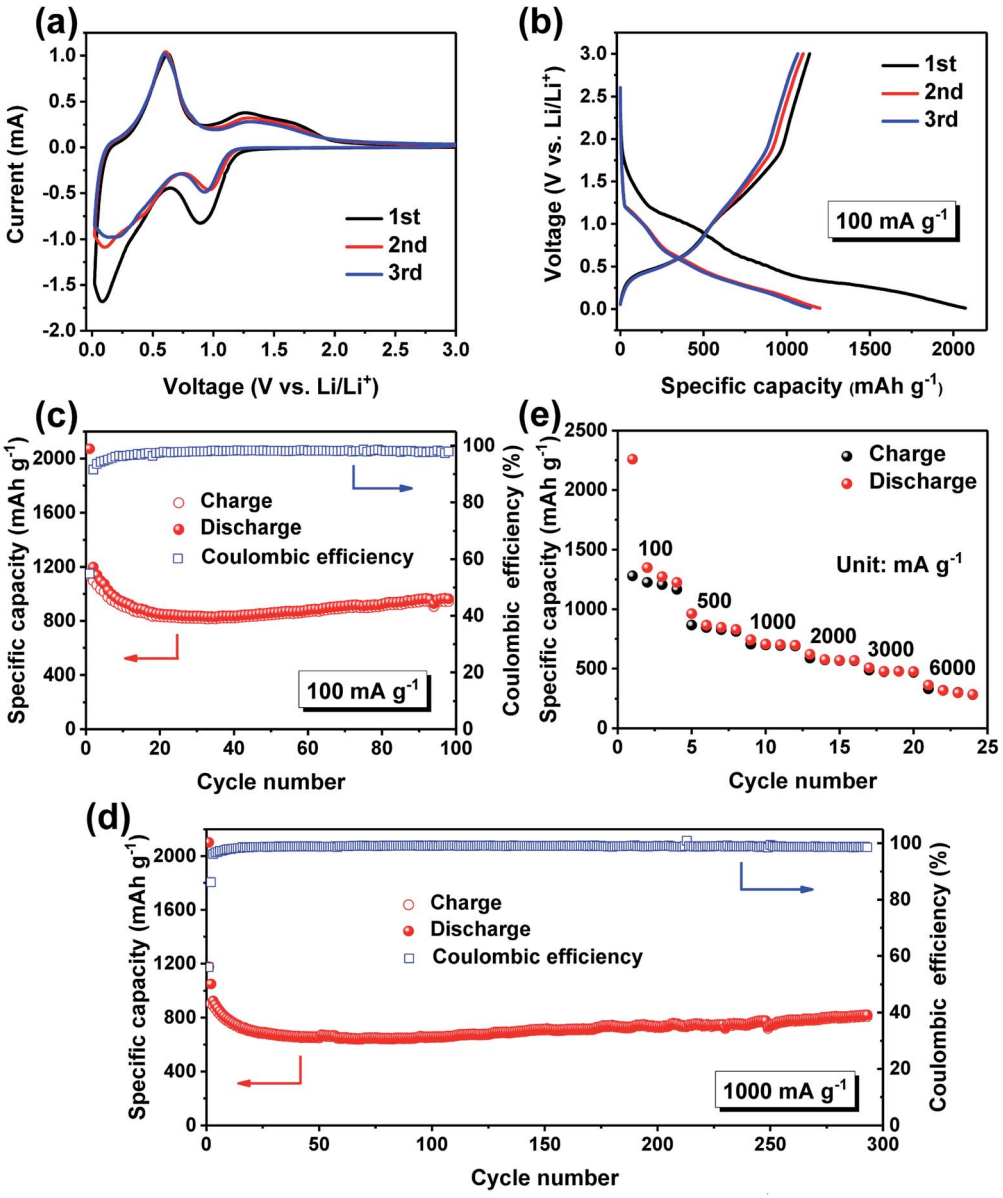

Fig. 4 (a) CV curves of the first three cycles at 0.1 mV s^{-1}, (b) galvanostatic charge–discharge curves for the first three cycles at 100 mA g^{-1}, (c and d) cycling performances at 100 and 1000 mA g^{-1}, (e) rate performances of the Sn/SnO sample.

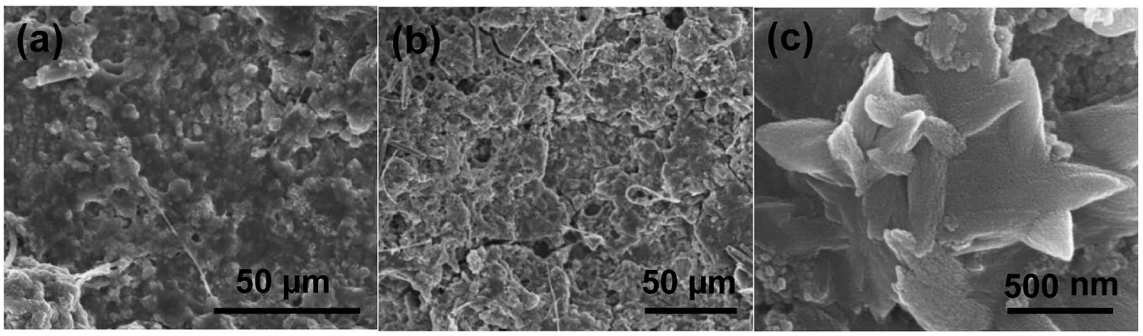

Fig. 5 SEM images of the Sn/SnO electrode (a) before cycling and (b and c) after 100 cycles at a current density of 100 mA g^{-1}.

Fig. 4c and d, respectively. As can be seen, the Sn/SnO electrode delivers a reversible discharge capacity as high as 964.1 mA h g^{-1} after 100 cycles at 100 mA g^{-1} (Fig. 4c). Furthermore, after the first few cycles, the CE quickly increases and stabilizes at around 98% for the subsequent cycles, demonstrating the superior reversibility and cycling stability. When the current density increases to 1000 mA g^{-1}, a discharge capacity of 820.4 mA h g^{-1} can still be obtained after 300 cycles, which is around 89% retention of the discharge capacity in the second cycle, revealing the excellent stability of the Sn/SnO electrode (Fig. 4d). Interestingly, the capacity fluctuation phenomenon can be obviously observed during the cycling test, which has already been reported for many metal oxide anodes.[11,46–48] This phenomenon may be mainly ascribed to the reversible formation/decomposition of an organic polymeric gel-like film on the electrode surface derived from the electrolyte decomposition, which could provide excess lithium ions storage sites. Fig. 4e depicts the rate capability of the Sn/SnO nanosheets at different current densities ranging from 100 to 6000 mA g^{-1}. It can be seen that the Sn/SnO nanosheets electrode exhibits outstanding rate capability with reversible discharge capacity of 1349.2, 961.8, 743.9, 620.0, 507.1 and 363.7 mA h g^{-1} at a current density of 100, 500, 1000, 2000, 3000 and 6000 mA g^{-1}, respectively.

The morphology changes of the electrode before cycling and after 100 cycles at 100 mA g^{-1} are presented in Fig. 5. It can be

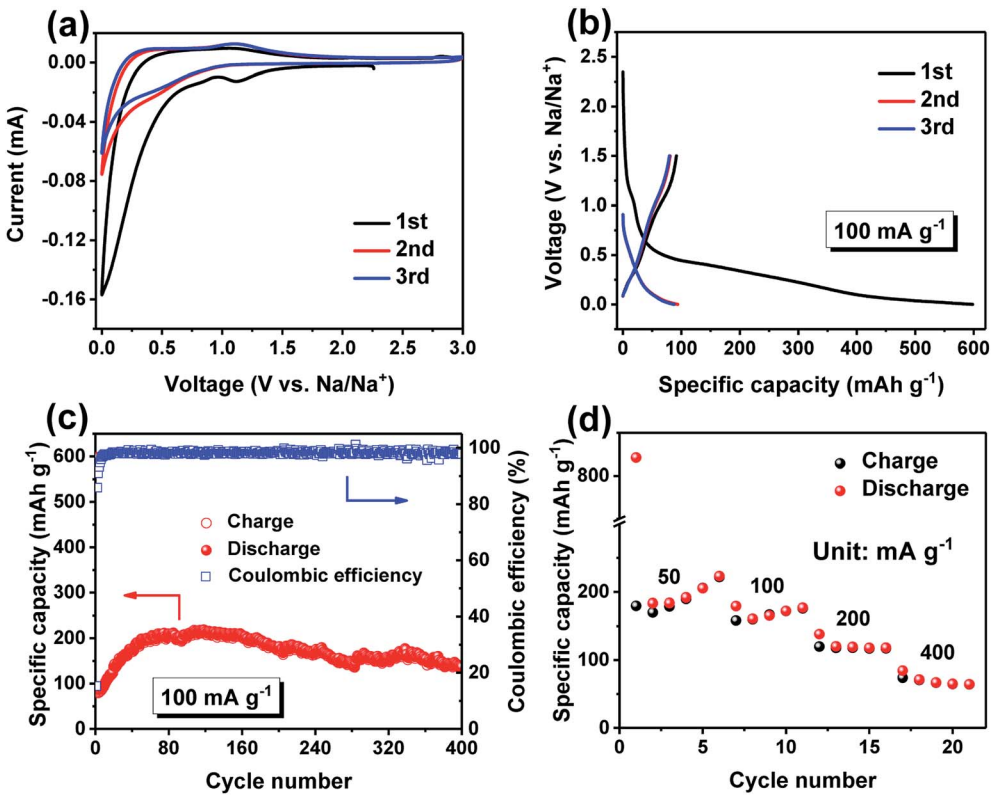

Fig. 6 (a) CV curves of the first three cycles at 0.1 mV s^{-1}, (b) galvanostatic charge–discharge curves for the first three cycles at 100 mA g^{-1}, (c) cycling performance at 100 mA g^{-1}, (d) rate performances of the Sn/SnO sample.

seen that the active material still remains homogenously distributed on the current collector with only some cracks appeared (Fig. 5a and b). Although the hollow spheres are hard to be observed, the Sn/SnO sample still preserves the sheet-like structure after long-time cycling (Fig. 5c).

The superior electrochemical performances of the Sn/SnO nanosheets can be attributed to the following factors. First, the peculiar hierarchical structure of nanosheets composed of hollow nanospheres can provide more lithium storage sites and shorter lithium electrons and ions transport length. Second, the hierarchical structure could help relieve the volume change. Third, the carbon layer leads to enhanced electrical conductivity and better structure stability.

The sodium storage properties of Sn/SnO anode were also investigated. Fig. 6a shows the CV curves of the Sn/SnO electrode for the first three cycles at a scan rate of 0.1 mV s^{-1} between 0.0 and 3.0 V. During the first cathodic scan, an irreversible peak at 1.1 V appeared, corresponding to the insertion of Na^+ into SnO and the formation of SEI film. The weak oxidation peaks in the charge process can be assigned to the reversible dealloying of Na_xSn.[49–51] From the second cycle, all the redox peaks have few changes, implying the high electrochemical reversibility of the Sn/SnO electrode. The representative charge–discharge curves for the initial three cycles of the Sn/SnO sample at 100 mA g^{-1} are depicted in Fig. 6b. The initial charge and discharge capacity are 246.9 and 831.1 mA h g^{-1}, respectively, corresponding to an ICE of 29.7%. The irreversible capacity loss could also be ascribed to the irreversible electrolyte decomposition and formation of SEI on the surface of electrode.[35,36] In the subsequent second and third cycles, the CE quickly increases to 97.5% and 92.2%, respectively. The corresponding cycling performance is presented in Fig. 6c. As can be seen, a reversible discharge capacity of 137.0 mA h g^{-1} could be delivered after 400 cycles. Specifically, after an evident increase for about 120 cycles, the specific capacity decreases slowly during the following cycles, indicating the material underwent an activated process. Such capacity increase has also been reported by Lu *et al.*[52] Fig. 6d illustrates the rate performances of the Sn/SnO electrode at different current densities from 50 to 400 mA g^{-1}. As can be seen, the electrode delivers a discharge capacity of 223.1, 179.6, 138.2 and 84.4 mA h g^{-1} at 50, 100, 200 and 400 mA g^{-1}, respectively. These results demonstrate the inspiring electrochemical performances of the Sn/SnO sample in SIBs.

4. Conclusions

In summary, we have successfully developed a facile hydrothermal method to synthesize hierarchical Sn/SnO nanosheets assembled by carbon-coated hollow nanospheres. When evaluated as an anode material for LIBs, the Sn/SnO sample exhibits excellent electrochemical properties. Specifically, a high reversible capacity of 2072.2 mA h g^{-1} was observed at 100 mA g^{-1} with 964.1 mA h g^{-1} retained after 100 cycles. Moreover, 820.4 mA h g^{-1} can be maintained during a long-term cycling at 1000 mA g^{-1} after 300 cycles along with a remarkable rate capability of 363.7 mA h g^{-1} at 6000 mA g^{-1}. Furthermore, the Sn/SnO sample also presents attractive sodium ion storage properties. Such superior electrochemical properties could be attributed to the unique architecture. On one hand, the peculiar hierarchical structure can not only provide more lithium storage sites, shorter lithium electrons and ions transport length but also help alleviate the volume variation as well as facilitate the electrolyte penetration. On the other hand, the carbon layer leads to enhanced electrical conductivity and better structure stability.

Conflicts of interest

There are no conflicts of interest to declare.

Acknowledgements

This work was supported by the National Natural Science Foundation of China (Grant No. 21878195, 21805198, 21805018), Distinguished Young Scholars of Sichuan University (2017SCU04A08) and Huohua Ku Project of Sichuan University (2018SCUH0094). Research Foundation for the Postdoctoral Program of Sichuan University (No. 2017SCU12018 and 2018SCU12045). Research Foundation for the Sichuan University and Zigong City Joint Research Project (2018CDZG-16). Thanks Dr Zhuo Zheng and for the help of data analysis.

References

1 N. Nitta, F. X. Wu, J. T. Lee and G. Yushin, *Mater. Today*, 2015, **18**, 252–264.
2 J. B. Goodenough and K. S. Park, *J. Am. Chem. Soc.*, 2013, **135**, 1167–1176.
3 B. Scrosati, J. Hassoun and Y. K. Sun, *Energy Environ. Sci.*, 2011, **4**, 3287–3295.
4 J. M. Tarascon and M. Armand, *Nature*, 2001, **414**, 359–367.
5 M. Winter, J. O. Besenhard, M. E. Spahr and P. Novák, *Adv. Mater.*, 2010, **10**, 725–763.
6 L. L. Wang, Q. F. Zhang, J. Y. Zhu, X. D. Duan, Z. Xu, Y. T. Liu, H. G. Yang and B. A. Lu, *Energy Storage Mater.*, 2019, **16**, 37–45.
7 T. Chen, Z. G. Wu, W. Xiang, E. H. Wang, T. R. Chen, X. D. Guo, Y. X. Chen and B. H. Zhong, *Electrochim. Acta*, 2017, **246**, 931–940.
8 L. Yu, H. B. Wu and X. W. Lou, *Adv. Mater.*, 2013, **25**, 2296–2300.
9 Z. G. Wu, Y. J. Zhong, J. Liu, J. H. Wu, X. D. Guo, B. H. Zhong and Z. Zhang, *J. Mater. Chem. A*, 2015, **3**, 10092–10099.
10 Z. S. Wu, W. C. Ren, L. Wen, L. B. Gao, J. P. Zhao, Z. P. Chen, G. M. Zhou, F. Li and H. M. Cheng, *ACS Nano*, 2010, **4**, 3187–3194.
11 C. Zhu, D. Wei, Y. Wu, Z. Zhang, G. Zhang, J. Duan, L. Li, H. Zhu, Z. Zhu and Z. Chen, *J. Alloys Compd.*, 2019, **778**, 731–740.
12 M. Sahoo and S. Ramaprabhu, *Carbon*, 2018, **127**, 627–635.
13 Y. Zhao, X. F. Li, B. Yan, D. B. Xiong, D. J. Li, S. Lawes and X. L. Sun, *Adv. Energy Mater.*, 2016, **6**, 19.

14 D. Saikia, J. R. Deka, C. J. Chou, H. M. Kao and Y. C. Yang, *J. Alloys Compd.*, 2019, **791**, 892–904.
15 C. Guan, X. Wang, Q. Zhang, Z. Fan, H. Zhang and H. J. Fan, *Nano Lett.*, 2014, **14**, 4852–4858.
16 W. Ren, C. Wang, L. Lu, D. Li, C. Cheng and J. Liu, *J. Mater. Chem. A*, 2013, **1**, 13433–13438.
17 Y. Q. Zhu, H. Z. Guo, H. Z. Zhai and C. B. Cao, *ACS Appl. Mater. Interfaces*, 2015, **7**, 2745–2753.
18 W. Su, Y. Liang and Y. Tang, *J. Alloys Compd.*, 2019, **801**, 402–408.
19 Z. Wang, D. Luan, F. Y. Boey and X. W. Lou, *J. Am. Chem. Soc.*, 2011, **133**, 4738.
20 C. H. Han, B. X. Zhang, K. N. Zhao, J. S. Meng, Q. He, P. He, W. Yang, Q. Li and L. Q. Mai, *Chem. Commun.*, 2017, **53**, 9542–9545.
21 Y. Wang, H. C. Zeng and J. Y. Lee, *Adv. Mater.*, 2006, **18**, 645–649.
22 H. Woo, S. Wi, J. Kim, J. Kim, S. Lee, T. Hwang, J. Kang, J. Kim, K. Park and B. Gil, *Carbon*, 2018, **129**, 342–348.
23 W. S. Kim, Y. Hwa, J. H. Jeun, H. J. Sohn and S. H. Hong, *J. Power Sources*, 2013, **225**, 108–112.
24 B. K. Cao, Z. Q. Liu, C. Y. Xu, J. T. Huang, H. T. Fang and Y. Chen, *J. Power Sources*, 2019, **414**, 233–241.
25 P. Gurunathan, P. M. Ette and K. Ramesha, *ACS Appl. Mater. Interfaces*, 2014, **6**, 16556–16564.
26 N. T. Wu, W. Z. Du, X. Gao, L. Zhao, G. L. Liu, X. M. Liu, H. Wu and Y. B. He, *Nanoscale*, 2018, **10**, 11460–11466.
27 S. Y. Hong, Y. Kim, Y. Park, A. Choi, N.-S. Choi and K. T. Lee, *Energy Environ. Sci.*, 2013, **6**, 2067–2081.
28 P. K. Nayak, L. Yang, W. Brehm and P. Adelhelm, *Angew. Chem., Int. Ed.*, 2018, **57**, 102–120.
29 J. Y. Hwang, S. T. Myung and Y. K. Sun, *Chem. Soc. Rev.*, 2017, **46**, 3529–3614.
30 N. Yabuuchi, K. Kubota, M. Dahbi and S. Komaba, *Chem. Rev.*, 2014, **114**, 11636–11682.
31 S. W. Kim, D. H. Seo, X. H. Ma, G. Ceder and K. Kang, *Adv. Energy Mater.*, 2012, **2**, 710–721.
32 V. L. Chevrier and G. Ceder, *J. Electrochem. Soc.*, 2011, **158**, A1011–A1014.
33 Z. Li, J. Feng, H. Hu, Y. Dong, H. Ren, W. Wu, Z. Hu and M. Wu, *J. Mater. Chem. A*, 2018, **6**, 18920–18927.
34 Z. Li, J. Ding and D. Mitlin, *Acc. Chem. Res.*, 2015, **48**, 1657–1665.
35 F. Zhang, J. Zhu, D. Zhang, U. Schwingenschlögl and H. N. Alshareef, *Nano Lett.*, 2017, **17**, 1302–1311.
36 B. Qin, H. Zhang, T. Diemant, D. Geiger, R. Raccichini, R. J. Behm, U. Kaiser, A. Varzi and S. Passerini, *ACS Appl. Mater. Interfaces*, 2017, **9**, 26797–26804.
37 P. Y. Chang and R. A. Doong, *J. Alloys Compd.*, 2019, **775**, 214–224.
38 J. Guo, P. Li, L. Chai, Y. Su, J. Diao and X. Guo, *RSC Adv.*, 2017, **7**, 30070–30079.
39 Y. Lee, M. R. Jo, K. Song, K. M. Nam, J. T. Park and Y.-M. Kang, *ACS Appl. Mater. Interfaces*, 2012, **4**, 3459–3464.
40 F. H. Du, Y. S. Liu, J. Long, Q. C. Zhu, K. X. Wang, X. Wei and J. S. Chen, *Chem. Commun.*, 2014, **50**, 9961–9964.
41 J. F. Wang and D. N. He, *Dalton Trans.*, 2018, **47**, 15307–15311.
42 J. Liang, X. Y. Yu, H. Zhou, H. B. Wu, S. Ding and X. W. Lou, *Angew. Chem., Int. Ed.*, 2014, **53**, 12803–12807.
43 Y. Cheng, Q. Li, C. Wang, L. Sun, Z. Yi and L. Wang, *Small*, 2017, **13**, 1701993.
44 Z. G. Wu, J. T. Li, Y. J. Zhong, J. Liu, X. D. Guo, L. Huang, B. H. Zhong and S. G. Sun, *J. Alloys Compd.*, 2015, **620**, 407–412.
45 J. F. Ye, H. J. Zhang, R. Yang, X. G. Li and L. M. Qi, *Small*, 2010, **6**, 296–306.
46 J. Liu, J. Xiao, X. Zeng, P. Dong, J. Zhao, Y. Zhang and X. Li, *J. Alloys Compd.*, 2017, **699**, 401–407.
47 G. Gao, S. Lu, B. Dong, Y. Xiang, K. Xi and S. Ding, *J. Mater. Chem. A*, 2016, **4**, 6264–6270.
48 C. J. Wu, Z. G. Wu, X. B. Zhang, R. Rajagopalan, B. H. Zhong, W. Xiang, M. Z. Chen, H. T. Li, T. R. Chen, E. H. Wang, Z. G. Yang and X. D. Guo, *ACS Appl. Mater. Interfaces*, 2017, **9**, 43596–43602.
49 X. Zhao, Z. Zhang, F. Yang, Y. Fu, Y. Lai and J. Li, *RSC Adv.*, 2015, **5**, 31465–31471.
50 Y. Wang, D. Su, C. Wang and G. Wang, *Electrochem. Commun.*, 2013, **29**, 8–11.
51 Y. X. Wang, Y. G. Lim, M. S. Park, S. L. Chou, J. H. Kim, H. K. Liu, S. X. Dou and Y. J. Kim, *J. Mater. Chem. A*, 2014, **2**, 529–534.
52 Y. C. Lu, C. Ma, J. Alvarado, T. Kidera, N. Dimov, Y. S. Meng and S. Okada, *J. Power Sources*, 2015, **284**, 287–295.

